



Research Article

Numerical investigation on comparative performance assessment of solar air heater with different artificial roughness elements in a triangular duct

Rafiuzzama SHAIK¹, Eshwaraiah PUNNA¹, S. K. GUGULOTHU^{2,*}

¹Department of Mechanical Engineering, GITAM University, Hyderabad, 502329, India

²Department of Mechanical Engineering, NIT Andhra Pradesh, Tadepalligudem, 534101, India

ARTICLE INFO

Article history

Received: 26 January 2023

Revised: 02 April 2023

Accepted: 29 April 2023

Keywords:

Artificial Roughness; Renewable Energy; Solar Air Heater; Triangular Duct and Reynolds Number

ABSTRACT

In this study, various roughness geometries on the absorber plate are examined to analyze their effects on fluid flow and heat transfer characteristics, focusing on parameters like the Nusselt number and friction factor. These geometries were examined in solar air heaters with triangular passages. The modified duct with different artificial roughness geometries is compared with a conventional triangular duct. In contrast to a smooth SAH, an increase in Nusselt number of 7.42 times and friction factor of 6.12 times is observed. With the increase of Reynolds number from 4000 to 20000, average Nusselt number and thermal performance parameters are increased in the case of semi-circular rib by 15.23% and 16.23% compared with the other roughness elements. The frictional penalty is decreased by 23.43% at maximum Re compared with the other roughness elements. The increase in frictional losses at lower Reynolds numbers is attributed to the reduced velocity of the airflow. Also, using semi-circular intrusions as artificial roughness, the Nusselt number value increases considerably, proving our innovation's capability. It is discovered that the suggested SAH with square and rectangular shaped rib performs better than traditional SAH under comparable shaped roughness components. However standard SAH is a superior choice for other roughness geometries.

Cite this article as: Shaik R, Punna E, Gugulothu SK. Numerical investigation on comparative performance assessment of solar air heater with different artificial roughness elements in a triangular duct. J Ther Eng 2025;11(1):49–61.

INTRODUCTION

A solar air heater (SAH) utilizes an absorber plate to transform a portion of solar energy into usable thermal output. However, due to the lesser capability of air to conduct the heat transfer lesser heat transfer enhancement is

observed. To enhance the heat transfer phenomenon significantly by maintaining the constant heat flux and constant temperature difference it is possible only with the help of artificial roughness inserted on the absorber plate [1-3]. As the roughness elements break up the viscous sub-layer on the absorber plate, more reattachment sites

*Corresponding author.

*E-mail address: santoshgk1988@gmail.com

This paper was recommended for publication in revised form by Editor-in-Chief Ahmet Selim Dalkılıç



are created, resulting in the improvement of Nu from the roughness elements to the air flow [3]. However, a negative consequence in the form of a more significant pressure drop is also seen, which boosts the SAH pumping power in rib-roughened cases. On the absorber plate, artificial roughness may be applied in a variety of ways [4-15]. Webb et al. [16] investigated the influence of circular rib with different range of parameters. They reported that the maximum Nusselt number (3.39) and minimum friction factor (2.38) is observed at relative roughness height (e/D) of 0.01 [17]. In the open literature similar results are observed [18] with the maximum thermal performance parameter (THPP) of 1.71. With grit type artificial roughness, the Nu_{avg} enhanced by 152% and TPP boosted by 12-36% [20]. Han et al. [21] investigated the impact of inclined ribs in a rectangular duct SAH. They reported that compared with other angle of attacks, 60° inclined rib developed the maximum normalised Nu . However, when the similar analysis is carried out in square duct the maximum heat transfer enhancement is observed in case of 45° inclined rib [22]. This is due to the slowing down of the secondary fluid flow produced by roughness elements moving in the direction of the side walls. In comparison with continuous ribs, discrete ribs allow the secondary flow to merge with main flow appropriately resulting in increase of flow velocity leading to better heat transfer performance [23].

Heat transfer phenomenon may be enhanced even with wire ribs by winding across the absorber plate in different ways, like V ribs [24-27], W-shape [28], and other patterns. The highest Nusselt number is found with V-shaped ribs compared to other roughness elements [29]. Liou et al. [30] studied the effects of artificial ribs and reported that square ribs achieved the maximum Nusselt number with

minimal frictional losses in comparison to other rib shapes. However, when the analysis is carried out experimentally, it is observed that the square ribbed elements have lesser penalty of friction (f_p) and higher Nu than the triangle rib [31]. Rokni et al. [32] numerically investigated the influence of ribs on two dimensional SAH model. They reported that when compared with 3D model, 2D models developed better heat transfer characteristics in case of chamfered roughness ribs. Soei et al. [33] investigated the influence of K-shaped ribs by theoretically developing the correlations to calculate the Nu and f_p . Maximum Nu is observed at relative pitch of 6.23. To validate the CFD code and the computational domain, quality of the grid and choosing the appropriate turbulence model are the two crucial components required [34]. Additionally, it is observed that the k- ϵ RNG model is the most effective in simulating turbulent flow in the SAH [35-37]. Only the V-shaped ribbed SAH has more than a $\pm 3\%$ discrepancy between the values anticipated using CFD models and the actual observations [38]. Korpale et al. [39] investigated the influence of rectangular ribs on the SAH. They reported that the optimal TPP value was 2.77 at 17.22 P/e and 0.044 e/D .

The open literature indicates that altering the flow passage (by adjusting the computational domain) and incorporating various artificial roughness elements can substantially enhance the performance of solar air heaters (SAH). This explanation served as the driving force for the authors' present inquiry, which examines the impact of different rib-roughness shapes to assess the SAH with triangle flow passage and attempts to pinpoint the optimal rib element geometry relative to other investigated geometries. Fewer research on alternative flow passages, including square and triangle. Very less research is carried out on the

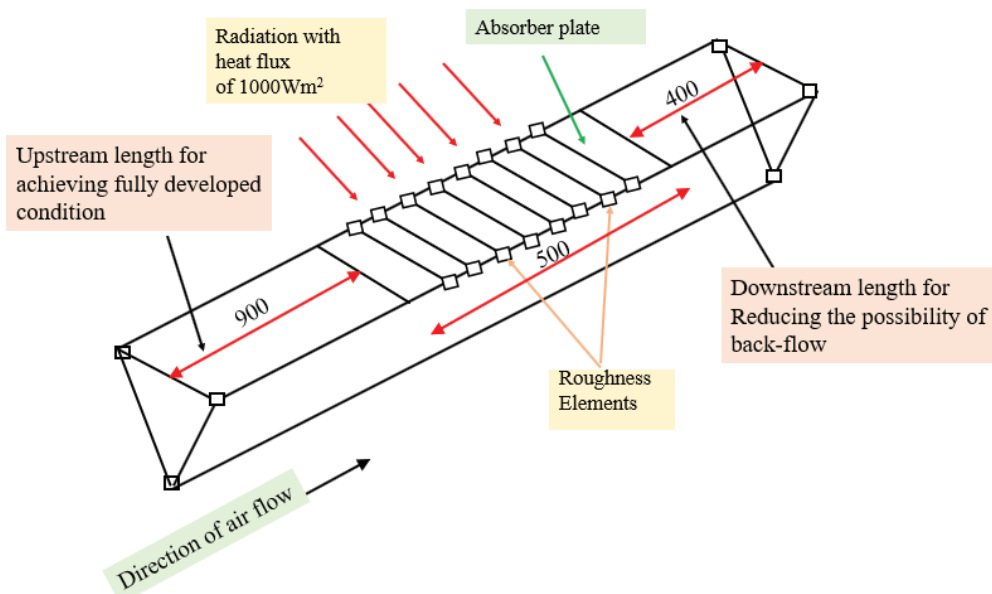


Figure 1. (a) Schematic Triangular SAH duct.

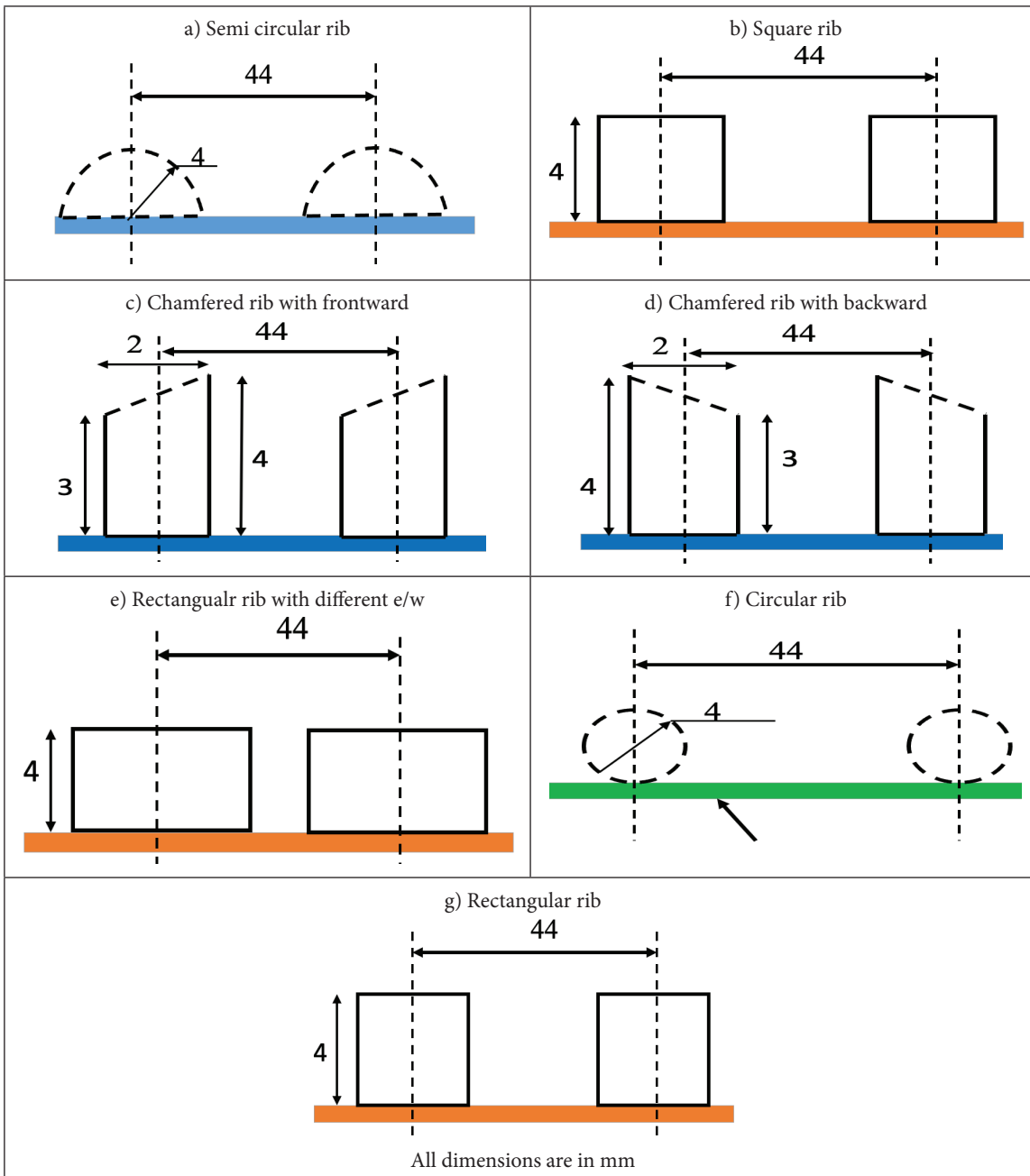


Figure 1. (b) Different roughness elements.

triangular duct SAH with different artificial roughness ribs. So, in this research, an effort is made to analyse the impact of different artificial ribs (rectangular rib with backward chamfered, rectangular rib with frontward chamfered, rectangular rib with various e/w , square rib, rectangular and semi-circular rib) on triangular duct to study the fluid flow physics and heat transfer in a systematic manner. The commercial software, ANSYS Fluent 18.1 is employed to simulate the flow domain. The impact of artificial roughness on triangular ducts with intrusions is studied to assess changes in velocity and temperature profiles.

PROBLEM DESCRIPTION

In a standard triangular duct, sharp corners cause flow deceleration. To improve airflow performance and enhance heat transfer, a new approach has been introduced. The solution has been analyzed by considering different artificial roughness ribs by modifying the Re number [55]. In the present case, seven different models are studied, which include different roughness elements on the triangular duct with the same geometry, as shown in Figure 1 (a&b). The optimal roughness geometry is found by creating roughness elements of

various forms and examining their effects in different geometries are considered for the analysis which is represented in Figure 1(b) with geometrical parameters. To analyze the fluid flow pattern, a triangular duct SAH of 0.9m upstream length followed by an absorber plate made of aluminum of 0.5 m length is considered [56]. To avoid the backflow from the exit of the absorber plate, a downstream length of 0.4 m is considered. A constant heat flux of 1000 W/m² is considered the energy input for the analysis. The simulations were run with the following presumptions to make good use of the computing resources [40-43]:

1. The flow of fluid is assumed to be steady and three-dimensional.
2. The fluid flow is incompressible all over the domain.
3. For both roughened and smooth ducts, a thin wall model is considered for the absorber plate.
4. Throughout the analysis, the thermo-physical properties of the absorber plate and flowing air is assumed to be constant.
5. The losses due to radiation are neglected.

Mesh Generation

Mesh impacts the precision, convergence, and speed of a simulation and produces effective solutions. The independent patch approach is used to the triangular cross-sectional duct to produce tetrahedral grids. The accuracy of the findings improves with finer meshing. The interaction between the solid and fluid creates a finer mesh as a result. Figure 2 shows a fine-grained mesh. For all ducts with heat-conducting surfaces, face sizing of a 5mm element size is used for a finer mesh. Each edge's size is specified independently, with element sizes ranging from 1.5mm to 4.33mm. Tetrahedral grids are made throughout the duct using a patch independent approach. The grid independence test is conducted to see if the numerical analysis described in the next section is accurate.

Computational Methodology

In order to study the fluid flow and thermal characteristics, the current computational domains for rectangular

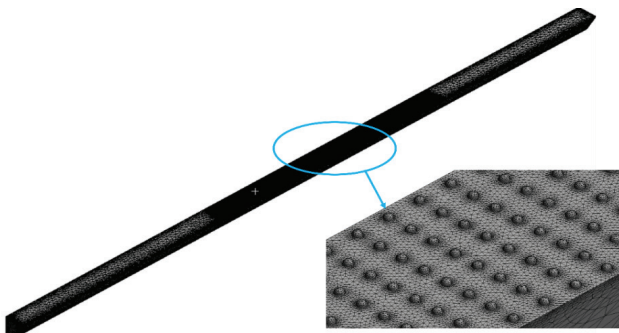


Figure 2. Pictorial view of meshing.

roughened, and smooth ducts are separated into structured quadrilateral elements (non-uniform).

Numerical equations employed

The principles of conservation, encompassing the continuity, momentum, and energy equations (1-3) [57], are solved utilizing ANSYS Fluent™ software, version 18.1.

$$\frac{\partial}{\partial x_i}(\rho \bar{u}_i) = 0 \quad (1)$$

$$\frac{\partial}{\partial x_i}(\rho \bar{u}_i \bar{u}_j) + \frac{\partial}{\partial x_i} \bar{P} = \frac{\partial}{\partial x_i} [(\mu + \mu_t) (\frac{\partial}{\partial x_i} (\bar{u}_i) + \frac{\partial}{\partial x_i} (\rho \bar{u}_j))] \quad (2)$$

$$C_p [\bar{u}_i \frac{\partial}{\partial x_i} (\rho \bar{T}) + \frac{\partial}{\partial x_i} (\frac{\mu_t}{Pr_t} \times \frac{\partial}{\partial x_i} \bar{T})] = \frac{\partial}{\partial x_i} (\lambda \times \frac{\partial}{\partial x_i} \bar{T}) \quad (3)$$

$$\frac{\partial(\rho k u_i)}{\partial x_i} - \frac{\partial}{\partial x_j} (\alpha_k \mu_{eff} \frac{\partial k}{\partial x_j}) - G_k + \rho \epsilon = 0 \quad (4)$$

$$\frac{\partial(\rho \epsilon u_i)}{\partial x_i} - \frac{\partial}{\partial x_j} (\alpha_k \mu_{eff} \frac{\partial \epsilon}{\partial x_j}) - C_{1\epsilon} \frac{\epsilon}{k} G_k + C_{2\epsilon} \frac{\epsilon^2}{k} \rho = R_\epsilon \quad (5)$$

Spatial discretization gradients are resolved using the least-squares cell method. To accurately capture the viscous sublayer, fine mesh elements are placed near the absorber plate, with quadrilateral cells discretized in non-uniform grids through CFD analysis. Tetrahedral mesh is selected for CR and SCR, while hexahedral elements are utilized for SR, BCRR, RR, and FCRR ribs [59]. Due to the pronounced gradients in the ribbed area.

Boundary Conditions

A wall boundary condition is assigned to both the insulated and absorber surfaces, while inlet and outlet boundary conditions are applied to the corresponding areas of the computational domain. Based on the Reynolds number range (4000 to 20000), the inlet pressure and temperature of the duct are set to 1 bar and 295 K, respectively. The duct walls are considered insulated, and a uniform heat flux of 1000 W/m² is applied to the roughened absorber plate [56].

RESULTS AND DISCUSSION

A solar air heater with different artificial roughness on absorber plate using intrusions by varying the Reynolds number is analysed. The obtained results are compared with fixed and smooth ribs working under identical conditions.

Validation of the Numerical Results

A GIT (grid independence test) is performed and it is mandatory to ensure for all cases that the thickness of the 1st layer corresponding to y+ should be equal to 1. The grid cells ranging from 410792 onwards are selected to conduct the CFD simulation, in order to ensure that the obtained results are grid independent [56]. It can be observed from Figure 3 that after 1505191 cells for the case of Reynolds number= 12,000, the percentage variations in average

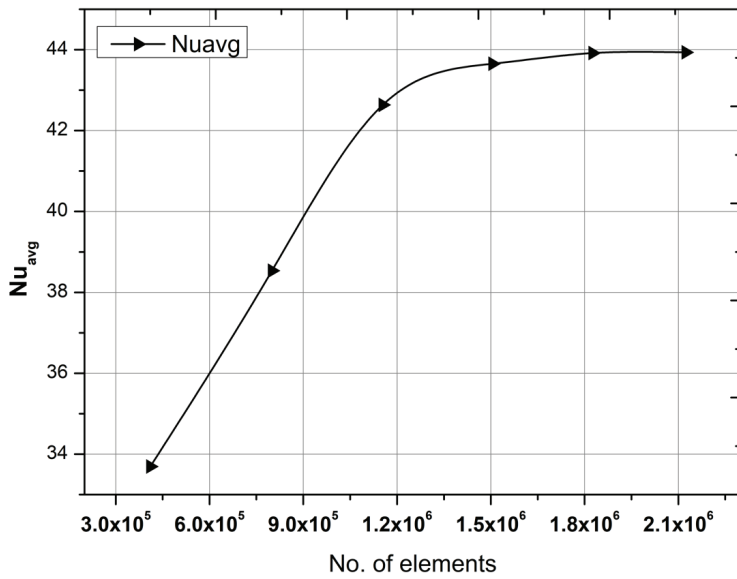


Figure 3. Grid independence test.

friction factor and Nusselt number were less than 0.5%. The deviation from 1825528 to 2123428 cells is 0.003%.

It is essential to choose appropriate turbulence models to validate the obtained results. To assess different turbulence models, simulations were performed on a conventional solar air heater [61]. Due to the small rib height relative to the duct height, fluid recirculation is limited to the region close to the absorber plate’s surface. Low-Reynolds number models were chosen for better accuracy near walls, as they are more effective in this region compared to high-Reynolds models [9,10]. This consideration influenced the selection of suitable turbulence models, with several RANS-based

models tested. Five turbulence models were applied across a Reynolds number range from 4000 to 20000 to estimate the Nusselt number. The results were validated against the Dittus-Boelter equation, as depicted in Figure 4. Findings revealed that the RNG model produced results closest to the theoretical Nusselt number. At low Reynolds numbers, the normalized Nusselt number (Nunorm) exhibited a maximum deviation of -6.45% compared to existing literature, while for higher Reynolds numbers, the deviation was less than 5%. These outcomes indicate that the selected mathematical models are both accurate and appropriate for the present study [47-50].

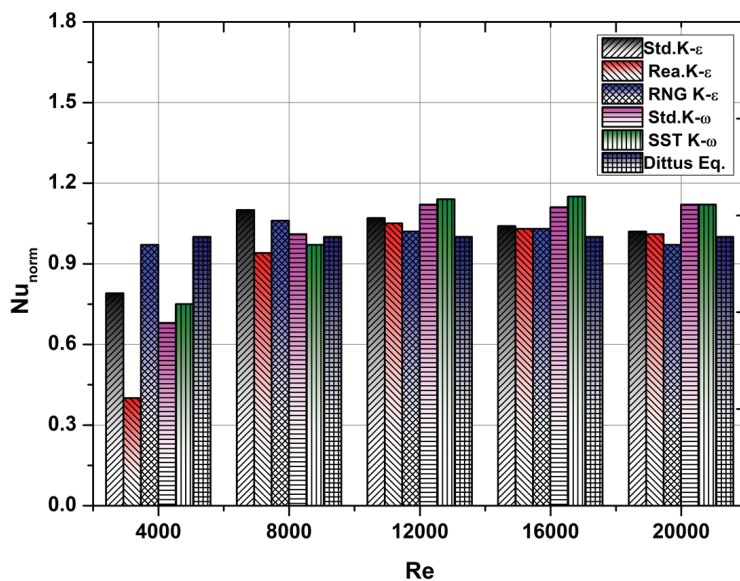


Figure 4. Validation of the proposed model.

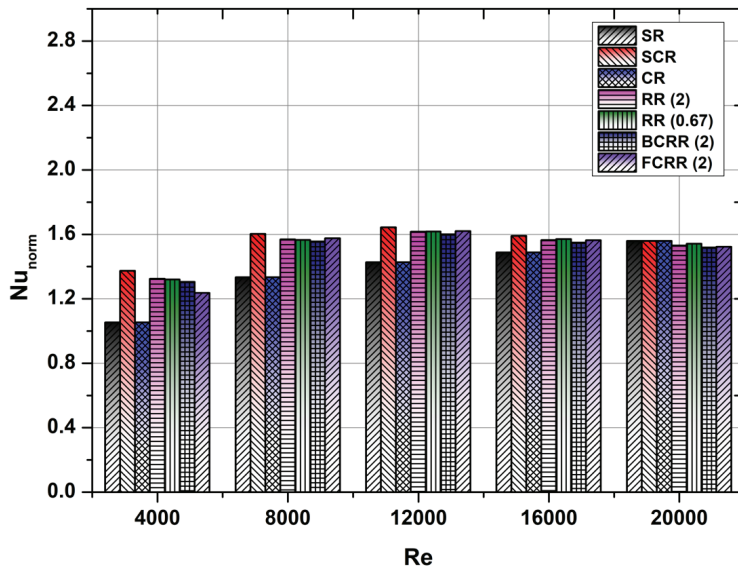


Figure 5. Influence of Nu_{norm} on different roughness elements.

Influence of Different Artificial Roughness Ribs on SAH

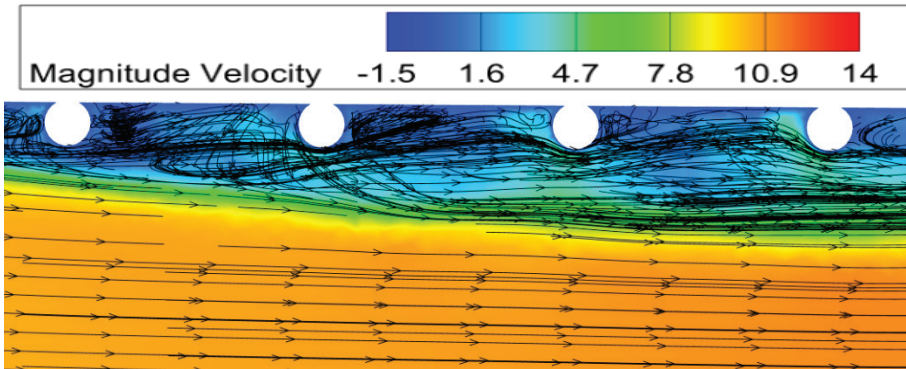
Figure 5 shows the effect of normalized Nusselt number across various roughness elements as the Reynolds number ranges from 4000 to 12000. It is observed that a significant improvement in heat transfer enhancement (Nu_{norm}) with an increase in the Re . At maximum Re of 20000, maximum Nu_{norm} is observed in all the roughness elements. When compared with SCR (6.42%) other elements like CR, SR, RR with different e/W , FCRR and BCRR developed lesser Nu_{norm} like 2.98%, 2.65%, 3.02%, 2.99%, 2.72%, 2.12% and 1.42% respectively. In case of FCRR with e/W 2 experiences poor augmentation due to least Nu_{norm} . Generally, better heat transfer takes place due to breaking up of viscous sub-layers caused by the rib-presence elements inserted above the surface of the plate. Additionally, the various re-attachment locations that the ribs produce across the absorber plate cause the flow to separate upstream of the rib element and reattach downstream of the rib element, which causes a significant change in random mixing of the fluid particles between two successive ribs. Local turbulence is shown to be more intense just after rib components [51–54]. The turbulence intensity significantly diminishes with increasing distance from the downstream rib, especially close to the rib surface. It is observed that maximum turbulence intensity of 16.23% is noted in SCR however least intensity is observed in BCRR with e/W of 2 (7.3%).

Another crucial characteristic that shows the flow configuration within the SAH duct is the rib-top surface. Due to ribs on the absorber plate greatly influences the fluid flow phenomenon resulting in recirculation of the fluid particles and increase in the reattachment lengths [34–35]. Figure 6 illustrates the variation of velocity streamlines for different roughness elements at a constant Re of 16000 [62]. It is observed that due to the presence of roughness

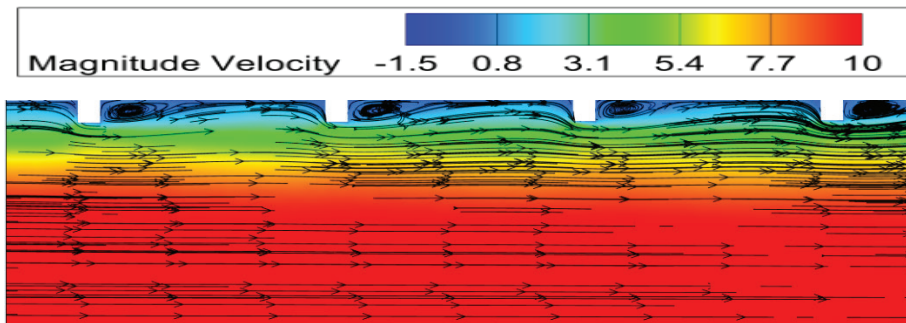
elements recirculation of fluid particles or secondary flow is developed near to the front and rear end of the rib element. However, stronger eddy formation is observed near to the rear end of the roughness elements rather than the front surface. As the roughness geometry is modified velocity streamline near to the surface of the absorber plate also changes. However, at FCRR with e/w of 2, the rib-top surface correctly directs the flow streamline avoiding the flow separation across the rib. Simultaneously, the rib-leading element's edge has a chamfered design that directs flow toward the centre, improving the random mixing of viscous layers into the mainstream resulting in the enhancement of convective heat transfer coefficient as shown in the Figure 7. The production of eddies when the flow is detached from the tip of the roughness elements in case of different shaped rib components leading to a decrease in the local between two ribs. As SCR and CR have no sharp edges, the streamlines run over the rib element without slightly perturbing the flow field, resulting in poor local turbulence intensity and a reduced local heat coefficient. As a result, the SCR and CR acquired a comparatively lesser Nu .

With an increase in the heat transfer phenomenon in case of artificial roughness elements SAH friction penalty also increases. Figure 8 illustrates the variation of f_p for different roughness elements at different Re . It is observed that with an increase in the Re higher f_p values are associated. With an increase in the Re drastic decrease in the f_p is achieved. The rib-element with corners (SR, RR with e/w and BCRR and FCRR) often has a higher f_p , compared with SCR and CR. For various shaped roughness-geometries, f_p in case of CR, SCRR, SR, RR, BCRR and FCRR are 1.96, 2.01, 2.98, 3.12, 3.23, and 3.74 respectively. Due to the development of drastic secondary flow in case of FCRR maximum fluctuation in f_p is observed. This can be

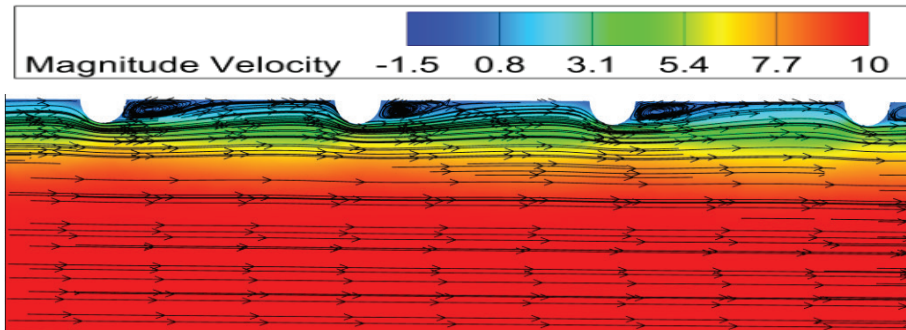
a)



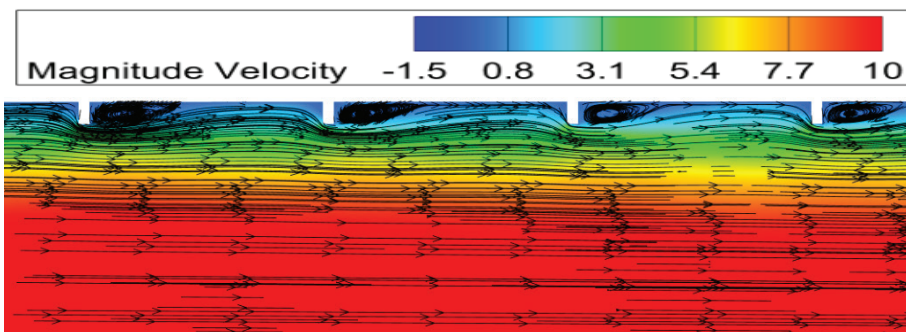
b)



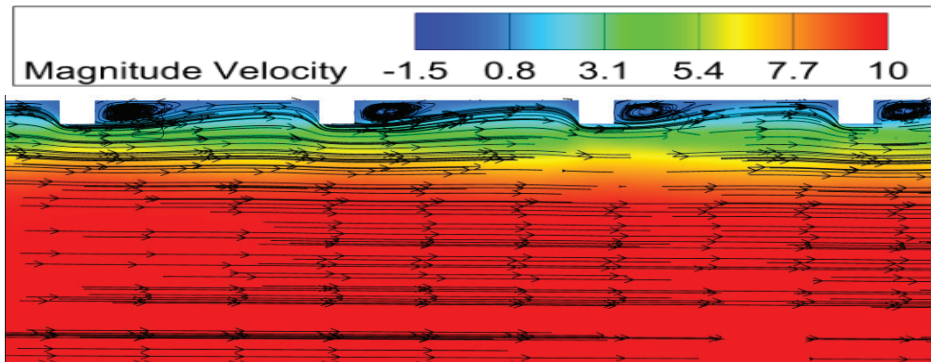
c)



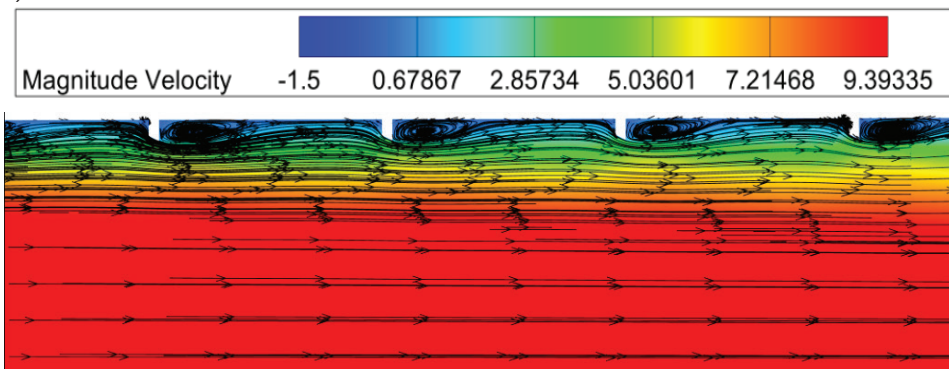
d)



e)



f)



g)

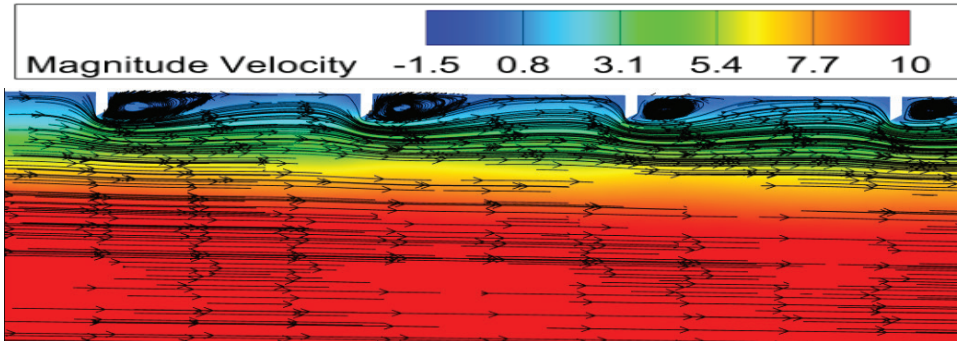


Figure 6. Velocity (m/s) profiles on different roughness elements.

decreased by reducing the pressure gradient in the opposite direction of the main stream.

The main objective of the modified SAH is to maximise the heat transfer phenomenon with minimum f_p . However, it is observed that with an increase in the Nu friction penalty also increased substantially. In order to assess the performance of the SAH the effective method is by obtaining the Nu_{norm} or f_p . The equation for the thermos hydraulic performance parameter (THPP), which must be calculated as a result, is given in equation. TPP defines that well-constructed SAH predominates f_p with an increase in the heat transfer phenomena. Figure 9 illustrates the variation of THPP with an increase in the Re for different roughness elements. It is observed that with an increase in the Re, THPP increased for all the roughness elements. At Re of

20000, maximum TPP is observed in case of SCR (2.99%) in comparison with the other roughness elements like CR, SR, RR with different e/W , BCRR and FCRR are 2.42%, 2.31%, 2.16%, 1.98%, 1.62% and 1.32% respectively. It is interesting to note that the greatest TPP and SCR correlate to the roughness geometry where both Nu_{norm} and f_p are maximal.

Impact of Velocity and Temperature Distributions

To prevent hot spot formation, the triangular duct is modified to three rounded-corner ducts. Figure 10(a) depicts how various roughness elements impact the local temperature gradient at maximum Reynolds number within the triangular duct. It is evident from Figure 10(a) that the highest temperatures are found on the surface,

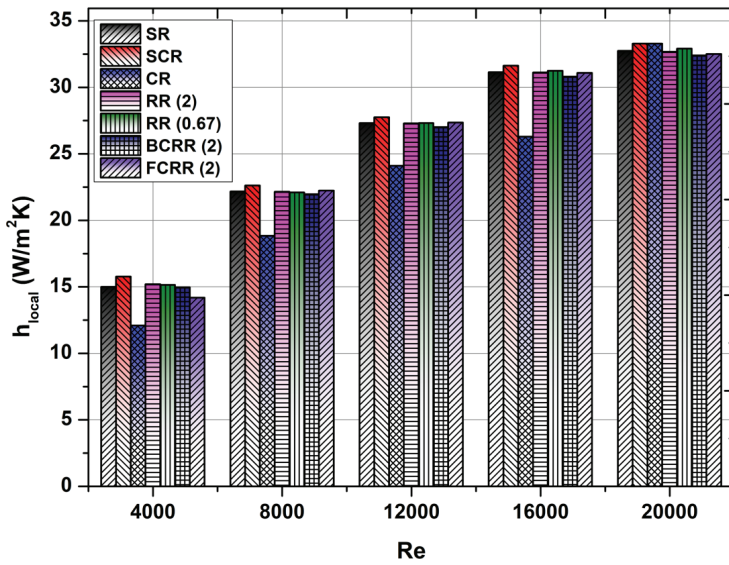


Figure 7. Influence of h_{local} on different roughness elements.

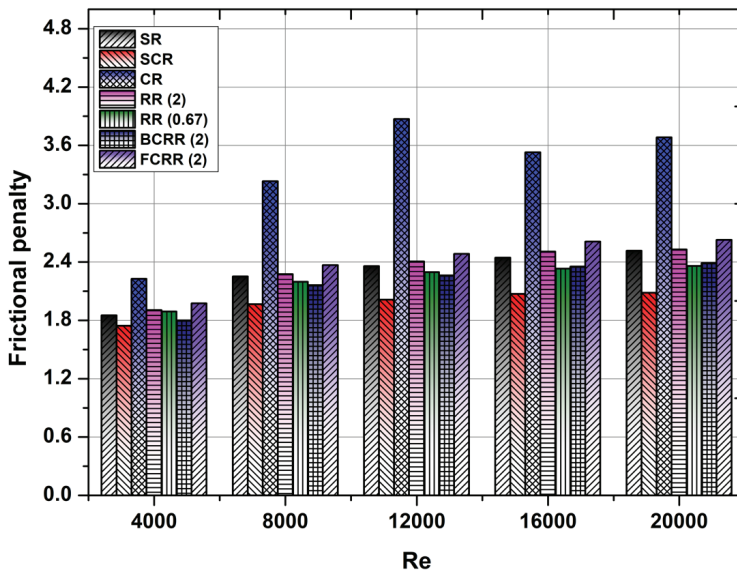


Figure 8. Influence of fp on different roughness elements.

decreasing towards the duct’s center, where the lowest temperatures occur across all roughness types. The presence of roughness elements increases surface area, enhancing interaction with fluid particles. Most fluid particles make contact with the heated surface [62]. Modifications to the conventional duct result in a minor temperature gradient at the center but show significant temperature variation at the duct corners. Intrusions thin the laminar sublayer, increasing turbulence and vortex formation, which enhances secondary heat transfer mechanisms [Prasad and Mullick, 1983]. Consequently, the temperature gradient remains nearly uniform from the corners toward the center.

Figure 10(b) illustrates the effect of different geometries on the local velocity gradient within the triangular duct at maximum Reynolds number. The highest velocity occurs at the duct’s center across all configurations [62]. However, in the conventional duct, sharp edges inhibit fluid mixing, leading to zero velocity at the solid-fluid interface. While all roughness elements achieve peak velocity at the center, in the CR configuration, maximum velocity is restricted to the central region, with a gradual reduction moving outward. When compared to the other elements SCR, the velocity profile is greater around the corners. In light of this, it can

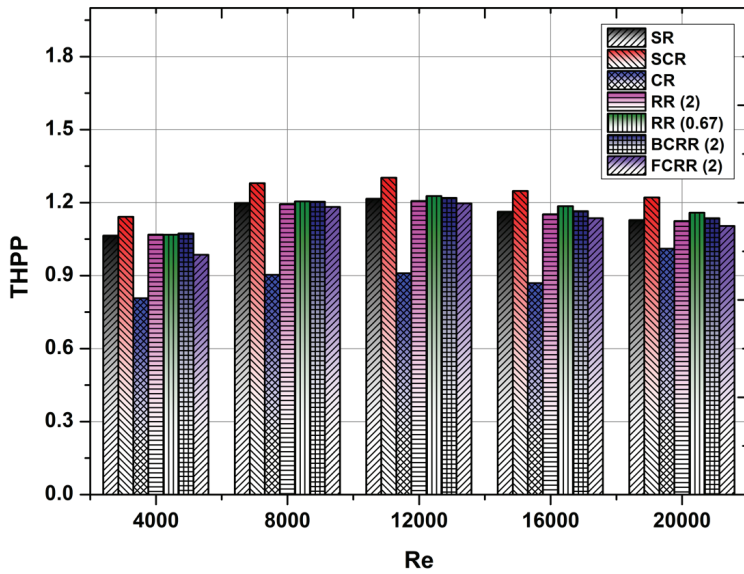


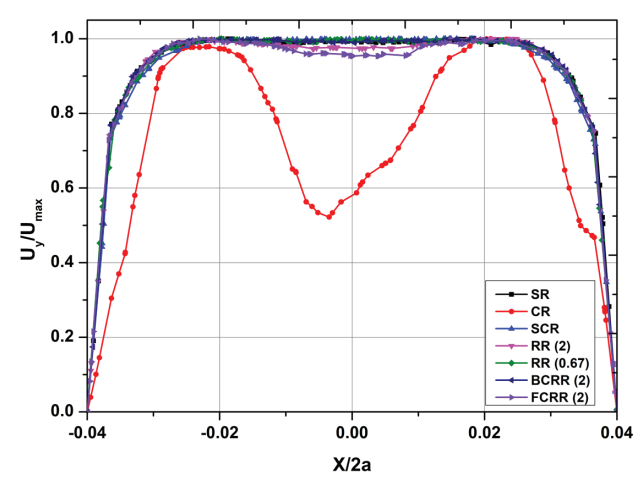
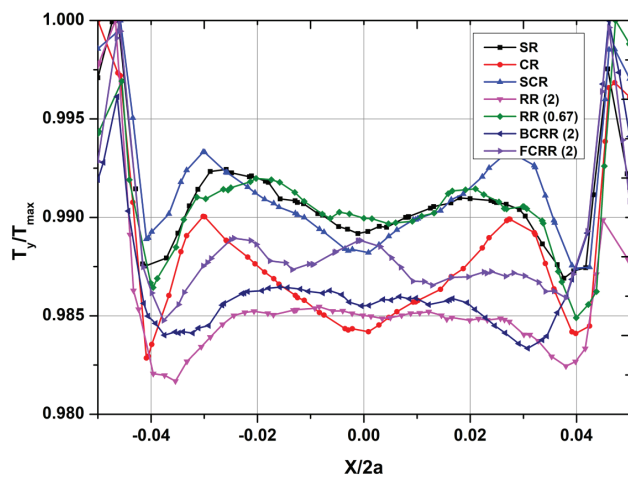
Figure 9. Influence of THPP on different roughness elements.

be said that the flow close may form in the corner’s rounded shape with roughened surface parts.

Validation of the Proposed Model with the Open Literature

The typical flow channel of a standard SAH is rectangular. It is observed that area of the SAH plays predominantly important role to enhance the heat transfer and the overall performance. Triangular cross-sectional SAH, also known as unusual SAH, is considered in the present research for this reason. In the present analysis comparison is done with the modified duct with the conventional duct in the open literature. Thus, this comparison can only be used to collect quantitative data. The comparison shows a significant fluctuation in Nu_{norm} and f_p when the parameters are slightly changed. It is observed that BCRR geometry

yielded the most significant value of Nu_{enh} for both SAH designs. However, in comparison with triangular duct the obtained f_p value [32] is three times larger than the rectangular duct. In case of rectangular duct better Nu_{norm} and f_p is obtained in case of CR and SR [18, 32, 42-46] which indicates that the heat transmission outweighs the friction penalty. The TPP levels reported by the various researchers do not agree, and a variance of around 10% is noted. From the proposed roughness elements, it is observed that the roughness elements which possess the sharp corners produced maximum TPP. This is due to an improvement in the secondary flow effectively mixing with primary flow improving heat transfer with minimal frictional cost. As a result, compared to traditional SAH, the suggested SAH yields the best TPP value.



a)

b)

Figure 10. Changes in Temperature and Velocity Profiles at $Z/I_{test} = 0.7$ with Re of 20000 for different models.

CONCLUSION

- 1 With the rib height being smaller than the duct height, fluid particle recirculation is restricted to the region close to the absorber plate's surface.
- 2 At lower Reynolds numbers, the predicted normalized Nusselt number (Nu_{norm}) shows a maximum discrepancy of -6.45% compared to available literature. For higher Reynolds numbers, however, the deviation in Nu_{norm} predictions remains below 5%.
- 3 In case of FCRR with $e/W = 2$ experiences poor augmentation due to least Nu_{norm} . Generally, better heat transfer takes place due to breaking up of viscous sub-layers caused by the rib-presence elements inserted above the surface of the plate.
- 4 As the distance from the downstream rib increases, the strength of the turbulence decreases drastically as it is near to the rib surface. It is observed that maximum turbulence intensity of 16.23% is noted in SCR however least intensity is observed in BCRR with e/W of 2 (7.3%).
- 5 The production of eddies when the flow is detached from the tip of the roughness elements in case of different shaped rib components leading to a decrease in the h_{local} between two ribs.
- 6 Modifications to the conventional duct result in a slight temperature gradient at the center, while noticeable temperature differences appear in all duct corners. The intrusions thin the laminar sublayer, increasing turbulence and encouraging vortex formation.
- 7 The circular rib (CR) has the poorest normalised Nu_{norm} which is 1.95, compared to other shaped roughness elements. In contrast, standard SAH is a superior choice for other roughness geometries.

Future Scope

- 1 In the SAH-duct domain, transverse vortex generators for improving heat transfer in duct flows have never been explored.
- 2 The rectangular SAH-aspect duct's ratio impact may be examined to see how it affects the SAH-functionality. duct's
- 3 The current analysis was conducted in a controlled, simulated environment using an electric heating plate; however, further research may allow for real-time operation under direct sunlight.
- 4 In the SAH-duct domain, higher ranges of Re may be examined to understand how they affect the thermal hydraulic performance.

NOMENCLATURE

SAH	Solar air heater
THPP	Thermal performance parameter
CFD	Computational Fluid dynamics
CR	Circular rib
SCR	Semicircular rib
RR	Rectangular rib

A	Duct area
C_p	Heat capacity
D_h	Dimeter
e/D_h	Relative height of roughness
f_p	Frictional penalty
h	Height of the triangular duct
h_{avg}	Average heat transfer coefficient
I	Turbulent Intensity
k	Turbulent Kinetic Energy
l_{test}	Length of test section
l_{inlet}	Length of entrance section
l_{outlet}	Length of exit section
Nu	Nusselt Number
Pr	Prandtl Number
Pr_t	Turbulent Prandtl Number
Re	Reynolds Number
T	Temperature

AUTHORSHIP CONTRIBUTIONS

Authors equally contributed to this work.

DATA AVAILABILITY STATEMENT

The authors confirm that the data that supports the findings of this study are available within the article. Raw data that support the finding of this study are available from the corresponding author, upon reasonable request.

CONFLICT OF INTEREST

The author declared no potential conflicts of interest with respect to the research, authorship, and/or publication of this article.

ETHICS

There are no ethical issues with the publication of this manuscript.

REFERENCES

- [1] Rao Y, Feng Y, Li B, Weigand B. Experimental and numerical study of heat transfer and flow friction in channels with dimples of different shapes. J Heat Transfer 2015;137:031901. [\[CrossRef\]](#)
- [2] Niu JL, Zhang LZ. Heat transfer and friction coefficients in corrugated ducts confined by sinusoidal and arc curves. Int J Heat Mass Transfer 2002;45:571-578. [\[CrossRef\]](#)
- [3] Zhang LZ. Turbulent three-dimensional air flow and heat transfer in a cross-corrugated triangular duct. J Heat Transfer 2005;127:1151-1158. [\[CrossRef\]](#)
- [4] Karabulut H, Ipci D, Cinar C. Numerical solution of fully developed heat transfer problem with constant wall temperature and application to isosceles triangle and parabolic ducts. Appl Therm Eng 2016;102:115-124. [\[CrossRef\]](#)

- [5] Kumar R, Kumar A. Computational fluid dynamics-based study for analyzing heat transfer and friction factor in semi-circular rib-roughened equilateral triangular duct. *Int J Numer Methods Heat Fluid Flow* 2017;27: 941-957. [\[CrossRef\]](#)
- [6] Kumar R, Goel V, Kumar A. Investigation of heat transfer augmentation and friction factor in triangular duct solar air heater due to forward facing chamfered rectangular ribs: A CFD based analysis. *Renew Energy* 2018;115:824-835. [\[CrossRef\]](#)
- [7] Kumar R, Kumar A. Experimental and computational fluid dynamics study on fluid flow and heat transfer in triangular passage solar air heater of different configurations. *J Sol Energy Eng* 2017;139:041013. [\[CrossRef\]](#)
- [8] Kumar R, Kumar A, Goel V. A parametric analysis of rectangular rib roughened triangular duct solar air heater using computational fluid dynamics. *Sol Energy* 2017;157:1095-1107. [\[CrossRef\]](#)
- [9] Bharadwaj G, Varun, Kumar R, Sharma A. Heat transfer augmentation and flow characteristics in ribbed triangular duct solar air heater: An experimental analysis. *Int J Green Energy* 2017;14:587-598. [\[CrossRef\]](#)
- [10] Masci R, Sciubba E. A lumped thermodynamic model of gas turbine blade cooling: prediction of first-stage blades temperature and cooling flow rates. *J Energy Resour Technol* 2018;140:020901. [\[CrossRef\]](#)
- [11] Forghan F, Askari O, Narusawa U, Metghalchi H. Cooling of turbine blade surface with expanded exit holes: Computational suction-side analysis. *J Energy Resour Technol* 2016;138: 4033590. [\[CrossRef\]](#)
- [12] Forghan F, Askari O, Narusawa U, Metghalchi H. Cooling of turbine blade surface with extended exit holes: Parametric study. *ASME Int Mech Eng Cong Expos* 2014;46514:V06AT07A043. [\[CrossRef\]](#)
- [13] Cebeci T, Bradshaw P. *Physical and Computational Aspects of Convective Heat Transfer*. Springer Science & Business Media; 1988. [\[CrossRef\]](#)
- [14] Sato N, Inagaki M, Kaneda K, Horinouchi N, Ota A. Numerical investigation of the effect of Prandtl number on heat transfer in a dimpled-channel flow. *Int J Heat Fluid Flow* 2017;68:139-150. [\[CrossRef\]](#)
- [15] Saqr KM, Kassem HI, Aly HS, Wahid MA. Computational study of decaying annular vortex flow using the $R\epsilon/k-\epsilon$ turbulence model. *Appl Math Model* 2012;36:4652-4664. [\[CrossRef\]](#)
- [16] Kabeel AE, Hamed MH, Omara ZM, Kandeal AW. Solar air heaters: Design configurations, improvement methods and applications - A detailed review. *Renew Sustain Energy Rev* 2017;70:1189-1206. [\[CrossRef\]](#)
- [17] Chhapparwal GK, Srivastava A, Dayal R. Artificial repeated-rib roughness in a solar air heater - A review. *Sol Energy* 2019;194:329-359. [\[CrossRef\]](#)
- [18] Sahu MK, Prasad RK. Exergy-based performance evaluation of solar air heater with arc-shaped wire roughened absorber plate. *Renew Energy* 2016;96:233-243. [\[CrossRef\]](#)
- [19] Wang CY. H2 forced convection for slip flow in an equilateral triangular duct. *J Thermophys Heat Transfer* 2014;28:100-104. [\[CrossRef\]](#)
- [20] Mortazavi SN, Hassanipour F. Effect of apex angle, porosity, and permeability on flow and heat transfer in triangular porous ducts. *J Heat Transfer* 2014;136:62227. [\[CrossRef\]](#)
- [21] Das D, Basak T. Role of distributed/discrete solar heaters during natural convection in the square and triangular cavities: CFD and heatline simulations. *Sol Energy* 2016;135:130-153. [\[CrossRef\]](#)
- [22] Li Z, Gao Y. Numerical study of turbulent flow and heat transfer in cross-corrugated triangular ducts with delta-shaped baffles. *Int J Heat Mass Transfer* 2017;108:658-670. [\[CrossRef\]](#)
- [23] Kumar R, Kumar A. Thermal and fluid dynamic characteristics of flow through triangular cross-sectional duct: A review. *Renew Sustain Energy Rev* 2016;61:123-140. [\[CrossRef\]](#)
- [24] Xie G, Li S, Zhang W, Sunden B. Computational fluid dynamics modeling flow field and side-wall heat transfer in rectangular rib-roughened passages. *J Energy Resour Technol* 2013;135:042001. [\[CrossRef\]](#)
- [25] Khir T, Jassim RK, Zaki GM. Application of exergoeconomic techniques to the optimization of a refrigeration evaporator coil with continuous fins. *J Energy Resour Technol* 2007;129:266-277. [\[CrossRef\]](#)
- [26] Singh S. Experimental and numerical investigations of a single and double pass porous serpentine wavy wiremesh packed bed solar air heater. *Renew Energy* 2020;145:1361-1387. [\[CrossRef\]](#)
- [27] Mahmood AJ. Thermal evaluation of a double-pass unglazed solar air heater with perforated plate and wire mesh layers. *Sustainability* 2020;12:3619. [\[CrossRef\]](#)
- [28] Perwez A, Kumar R. Thermal performance investigation of the flat and spherical dimple absorber plate solar air heaters. *Sol Energy* 2019;193:309-323. [\[CrossRef\]](#)
- [29] Talukdar P, Shah M. Analysis of laminar mixed convective heat transfer in horizontal triangular ducts. *Numer Heat Transfer Part A: Appl* 2008;54:1148-1168. [\[CrossRef\]](#)
- [30] Sasmito AP, Kurnia JC, Wang W, Jangam SV, Mujumdar AS. Numerical analysis of laminar heat transfer performance of in-plane spiral ducts with various cross-sections at fixed cross-section area. *Int J Heat Mass Transfer* 2012;55:5882-5890. [\[CrossRef\]](#)
- [31] Rokni M, Gatski TB. Predicting turbulent convective heat transfer in fully developed duct flows. *Int J Heat Fluid Flow* 2001;22:381-392. [\[CrossRef\]](#)

- [32] Kumar A, Kim MH. Thermohydraulic performance of rectangular ducts with different multiple V-rib roughness shapes: A comprehensive review and comparative study. *Renew Sustain Energy Rev* 2016;54:635-652. [\[CrossRef\]](#)
- [33] Daschiel G, Frohnafel B, Jovanović J. Numerical investigation of flow through a triangular duct: The coexistence of laminar and turbulent flow. *Int J Heat Fluid Flow* 2013;41:27-33. [\[CrossRef\]](#)
- [34] Kumar R, Kumar A, Goel V. A parametric analysis of rectangular rib roughened triangular duct solar air heater using computational fluid dynamics. *Sol Energy* 2017;157:1095-1107. [\[CrossRef\]](#)
- [35] Goel V, Guleria P, Kumar R. Effect of apex angle variation on thermal and hydraulic performance of roughened triangular duct. *Int Commun Heat Mass Transfer* 2017;86:239-244. [\[CrossRef\]](#)
- [36] Obot NT, Adu-Wusu K. The flow pattern in a scalene triangular duct having two rounded corners. 1985. [\[CrossRef\]](#)
- [37] Ray S, Misra D. Laminar fully developed flow through square and equilateral triangular ducts with rounded corners subjected to H1 and H2 boundary conditions. *Int J Therm Sci* 2010;49:1763-1775. [\[CrossRef\]](#)
- [38] Kline SJ. Describing uncertainty in single sample experiments. *Mech Eng* 1953;75:3-8.
- [39] Tu J, Yeoh GH, Liu C. *Computational Fluid Dynamics: A Practical Approach*. 2nd ed. Butterworth-Heinemann Elsevier UK; 2013.
- [40] Fluent A. 18.1 Theory's Guide. 2018.
- [41] Abhay L, Chandramohan VP, Raju VRK. Numerical analysis on solar air collector provided with artificial square shaped roughness for indirect type solar dryer. *J Clean Prod* 2018;190:353-367. [\[CrossRef\]](#)
- [42] Kumar R, Kumar A, Goel V. Numerical simulation of flow through equilateral triangular duct under constant wall heat flux boundary condition. *J Inst Eng India Ser C* 2017;98:313-323. [\[CrossRef\]](#)
- [43] Rao Y, Feng Y, Li B, Weigand B. Experimental and numerical study of heat transfer and flow friction in channels with dimples of different shapes. *J Heat Transfer* 2015;137:4029036. [\[CrossRef\]](#)
- [44] Sato N, Inagaki M, Kaneda K, Horinouchi N, Ota A. Numerical investigation of the effect of Prandtl number on heat transfer in a dimpled-channel flow. *Int J Heat Fluid Flow* 2017;68:139-150. [\[CrossRef\]](#)
- [45] Kumar R, Goel V, Kumar A. A parametric study of the 2D model of solar air heater with elliptical rib roughness using CFD. *J Mech Sci Technol* 2017;31:959-964. [\[CrossRef\]](#)
- [46] Ligrani PM, Harrison JL, Mahmmud GI, Hill ML. Flow structure due to dimple depressions on a channel surface. *Phys Fluids* 2001;13:3442-3451. [\[CrossRef\]](#)
- [47] Kumar R, Khurana S, Kumar A, Goel V. Effect of dimple intrusions and curvature radius of rounded corner triangular duct on fluid flow and heat transfer. *J Therm Sci Eng Appl* 2019;11:031001. [\[CrossRef\]](#)
- [48] Saqr KM, Kassem HI, Aly HS, Wahid MA. Computational study of decaying annular vortex flow using the $Re/k-\epsilon$ turbulence model. *Appl Math Model* 2012;36:4652-4664. [\[CrossRef\]](#)
- [49] Yadav AS, Sharma SK. Numerical simulation of ribbed solar air heater. In: *Advances in Fluid and Thermal Engineering: Select Proceedings of FLAME 2020*. Springer Singapore; 2021. pp. 549-558. [\[CrossRef\]](#)
- [50] Yadav AS, Alam T, Gupta G, Saxena R, Gupta NK, Allamraju KV, et al. A numerical investigation of an artificially roughened solar air heater. *Energies* 2022;15:8045. [\[CrossRef\]](#)
- [51] Manca O, Nardini S, Ricci D, Tamburrino S. Numerical investigation on nanofluid mixed convection in triangular ducts heated by a uniform heat flux. *Eng Syst Des Anal* 2012;44854:497-506. [\[CrossRef\]](#)
- [52] Bezbaruah PJ, Das RS, Sarkar BK. Overall performance analysis and GRA optimization of solar air heater with truncated half conical vortex generators. *Sol Energy* 2020;196:637-652. [\[CrossRef\]](#)
- [53] Kumar R, Goel V. Unconventional solar air heater with triangular flow-passage: A CFD based comparative performance assessment of different cross-sectional rib-roughnesses. *Renew Energy* 2021;172:1267-1278. [\[CrossRef\]](#)
- [54] Khandelwal N, Sharma M, Singh O, Shukla AK. Recent developments in integrated solar combined cycle power plants. *J Therm Sci* 2020;29:298-322. [\[CrossRef\]](#)
- [55] Misra R, Singh J, Jain SK, Faujdar S, Agrawal M, Mishra A, Goyal PK. Prediction of behavior of triangular solar air heater duct using V-down rib with multiple gaps and turbulence promoters as artificial roughness: A CFD analysis. *Int J Heat Mass Transfer* 2020;162:120376. [\[CrossRef\]](#)
- [56] Raju LB, Sastry GR, Gugulothu SK, Kumar R, Balakrishnan D. Computational analysis on solar air heater with combination of alternate dimple protrusions and intrusions on absorber plate with one rounded corner triangular duct. *Environ Sci Pollut Res* 2022;1-16. [\[CrossRef\]](#)